Investigation on the mechanical properties of 3D printed hybrid continuous fiber-filled composite considering influence of interfaces

Shixian Li, Kui Wang, Wanying Zhu, Yong Peng, Said Ahzi, Francisco Chinesta

Investigation on the mechanical properties of 3D printed hybrid continuous fiber-filled composite considering influence of interfaces

Shixian Li[1,2] · Kui Wang[1] · Wanying Zhu[1] · Yong Peng[1] · Said Ahzi[2] · Francisco Chinesta[3]

Fused deposition modeling (FDM) is a promising additive manufacturing technique for fabrication of continuous fiber-reinforced thermoplastic composites. For composite applications, the balance of material properties, including rigidity and toughness, needs to be considered. To overcome the drawbacks induced by single continuous fiber reinforcement, this study focused on the design and characterization of hybrid continuous fiber (continuous carbon and Kevlar fibers)-reinforced polyamide (PA)-based composites, prepared by 3D printing, to achieve comprehensive performance improvements and designable mechanical properties. The deformation and failure behaviors with the effects of hybrid conception, stacking sequences, and raster orientations of composites were investigated. A hybrid effect model was introduced to evaluate the hybrid effect of 3D printed continuous fiber-filled composites. Besides, compared to composites fabricated via conventional methods, a major difference in 3D printed hybrid composites is the performance of interfacial bonding. A roller peeling test was therefore conducted to investigate the interfacial strength of different materials. An analytical approach was developed to predict the tensile modulus of the printed hybrid composites by introducing an interfacial strengthening coefficient into the volume average stiffness model. The combined experimental and predicted results showed that hybrid composite specimens with separated distribution sequence showed a higher tensile modulus compared to hybrid composites with concentrated distribution. The higher tensile properties of the printed hybrid composites with separated continuous fiber-reinforced layers were attributed to the strong interfacial bonding, which delayed crack initiation and propagation.

Keywords Fused deposition modeling · Hybrid continuous fiber · Hybrid effect model · Stacking sequence · Raster orientation · Prediction model · Interfacial properties

1 Introduction

3D printing, also known as additive manufacturing (AM), is one of the most promising techniques for manufacturing components with complex geometries [1]. It can produce intricate parts with less cost and without using special tools compared to traditional manufacturing technologies. The fused deposition method (FDM), a technique for fabricating objects by layering extruded molten thermoplastic materials, is one of the most common AM approaches applied in commercial 3D printers due to its low cost, simple operation, low material waste, and environmental friendliness [2, 3]. Despite the numerous printing polymers available such as acrylonitrile butadiene styrene (ABS), polylactic acid (PLA), and polyamide (PA), the stiffness and strength of these pristine thermoplastics are relatively weak for structural purposes [4–6].

In recent years, reinforced fillers such as continuous fibers are widely used in FDM to improve the mechanical behaviors of 3D printed thermoplastic-based composites. In the literature, Mei et al. [7],Van Der Klift et al. [8], Heidari-Rarani et al. [9], Dickson et al. [10], and Wang et al. [11] found that the addition of single continuous fiber often increased some mechanical properties of composites but at the same time decreased other mechanical behaviors. However, for composite applications, the balance of materials properties needs to be

✉ Kui Wang
kui.wang@csu.edu.cn

[1] Key Laboratory of Traffic Safety On Track of Ministry of Education, School of Traffic & Transportation Engineering, Central South University, Changsha 410075, China

[2] ICUBE Laboratory–CNRS, University of Strasbourg, 67000 Strasbourg, France

[3] ESI Chair, PIMM, Arts Et Métiers Institute of Technology, 75013 Paris, France

considered [12]. To overcome the drawbacks induced by single reinforcement, composites prepared via conventional methods such as inclusion-filled polymers or woven/non-woven fabrics usually used a hybrid concept by adding two or more types of fibers to have comprehensive performance improvements and designable mechanical properties [13–15]. In our previous studies, we have found that the simultaneous use of multi-type continuous fibers with different properties was an effective method to tailor the mechanical behaviors of composites manufactured by 3D printing [16, 17].

However, compared to traditional manufacturing methods, the interface influences would be more important for the FDM approach due to less printing pressure [18–22]. Peng et al. [18] found that the mechanical properties of composites were higher when stacked continuous carbon fiber-reinforced layers (CCFRLs) were separated in composites. This phenomenon was attributed to the much stronger adhesion of initial interfaces for separated specimens than concentrated ones. Yavas et al. and Touchard et al. [19, 20] discovered that the interfacial bonding strength between printed layers of 3D printed composites played an important role in mechanical properties. Meanwhile, Li et al. [23], Araya-Calvo et al. [24], Parmiggiani et al. [25], and Chacón et al. [26] discovered that the mechanical properties of 3D printed continuous fiber-filled composites highly depended on printing parameters. For 3D printed hybrid composites, the mechanical properties therefore would not only depend on the properties of each reinforcement fiber but also on the printing parameters as well as interactions between different printed filaments and layers. As a result, it is essential to investigate the contributions of interface properties affected by hybrid fiber reinforcement as well as printing parameters to the mechanical performance of 3D printed continuous fiber composites.

In this work, the mechanical behaviors of PA-based continuous carbon and Kevlar fiber-reinforced non-hybrid and hybrid composites fabricated via 3D printing were studied. The influences of different printing designs on tensile and interfacial properties of non-hybrid and hybrid composites were systematically investigated. The deformation and failure behaviors with the effects of hybrid conception, stacking sequences, and raster orientations of composites were investigated by fractography. A hybrid effect model and a prediction model considering interface contributions were introduced to analyze the hybrid effect and to predict the tensile modulus of printed hybrid composites.

2 Experimental methodologies

2.1 Materials and processing

In this study, polyamide (PA) filaments (1.75 mm, density of 1.1 g/cm^3) were chosen as the thermoplastic matrix. Carbon fibers are known for high strength and stiffness but poor toughness, while Kevlar fibers are known for their high strain to failure properties but relatively low strength. Therefore, continuous carbon fiber (CCF) filaments (0.38 mm, density of 1.4 g/cm^3) and continuous Kevlar fiber (CKF) filaments (0.32 mm, density of 1.2 g/cm^3), supplied by Markforged®, were chosen as hybrid reinforcements. Note that the CCF and CKF filaments were not clusters of pure continuous fibers. The reinforced continuous fiber filaments were composed of continuous carbon or Kevlar fiber bundles infused with a large amount of a thermoplastic PA sizing agent [27]. Specifically, after the thermogravimetric analysis (TGA), it was found that the CCF and CKF in the filaments corresponded to 47.98 and 40.85 wt.%, respectively [17, 28]. Prior to use, all the materials were stored in a dry box to minimize the environment humidity.

The MarkForged® Mark7 3D printing equipment (Markforged, Cambridge, MA, USA) for the manufacturing process of continuous fiber-reinforced composites was adopted in this study. The printer included two extrusion heads, allowing for the printing of the thermoplastic matrix and continuous fiber filaments independently. The extrusion temperatures of the continuous fiber filaments and matrix filaments were 270 ℃ and 255 ℃, respectively. The printed composites were deposited onto a non-heated printing platform.

2.2 Tensile test

Tensile test specimens with different raster orientations (0°/90°, ± 45°) and stacking sequences (concentrated or separated distribution) of continuous fiber layers were prepared, as shown in Fig. 1. Note that the 0°-continuous fiber raster orientation coincided with the x-axis and the 90°-continuous fiber raster orientation coincided with the *y*-axis. Rectangular specimens with dimensions of 80.0 mm × 5.0 mm × 1.0 mm were selected according to the ASTM D3039 standard. Each specimen had eight printed layers including four continuous fiber layers (continuous Kevlar fiber-reinforced layers, CKFRLs, and continuous carbon fiber-reinforced layers, CCFRLs) and four matrix layers (polyamide layers, PALs). In the following definitions, non-hybrid and hybrid printed composites with concentrated and separated distribution of CCFRLs and/or CKFRLs were defined as CD and SD specimens, respectively. For example, specimens with 0° continuous carbon fiber raster orientation, 90° continuous Kevlar fiber raster orientation, as well as separated distribution of CCFRLs and CKFRLs were named as 0°-CCFRPA/90°-CKFRPA-SD. The rest of the specimens could be named in the same way. The volume consumptions of printing filaments for

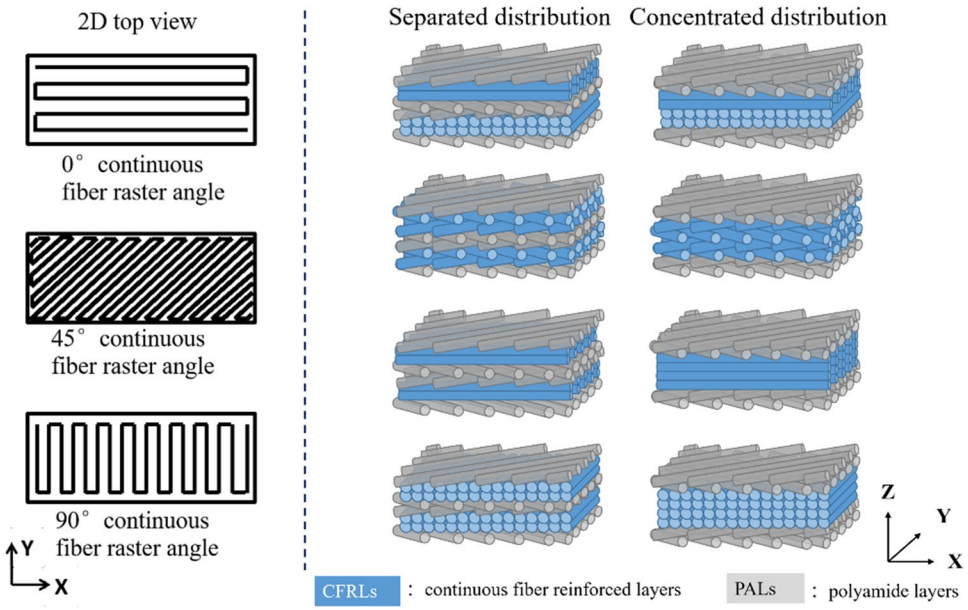

Fig. 1 Schematic presentation of printed continuous fiber-filled composites with different continuous fiber raster angles and different stacking sequences

each layer were computed, as listed in Table 1. The volume fractions of continuous fiber filaments could be therefore calculated, as also shown in Table 1.

The mechanical behaviors of the 3D printed continuous fiber-filled hybrid and non-hybrid composites were investigated by tensile testing using an MTS universal mechanical testing machine (E44, MTS Co., USA) with a 30-kN loading cell. After clamping the specimens, a cross-head loading rate of 10 mm/min was applied at room temperature. The maximum stress was taken as the tensile strength. Note that each measurement was averaged from the results of three repeated and recorded tests.

2.3 Roller peeling test

The specimens for the roller peeling test were prepared according to the ASTM D3167 standard, consisting of rigid and flexible parts, as shown in Fig. 2(a). Note that the continuous fibers in the peeling test specimens were printed by 0° raster orientation [29]. In this work, we used the tape to set up an artificial pre-crack zone between the adjacent layers during the printing process, following a similar study reported in the literature. Specifically, in the C-K specimen, the tape was placed after the Kevlar fiber layer printing and before the carbon fiber layer printing. In the following definitions, PA-PA, C–C, K-K, C-K, C-PA, and K-PA represented

Table 1 Filament volume consumption and volume fraction for the non-hybrid and hybrid printed composites

Specimens		Ply number in specimens			Filament volume consumption per ply (cm^3)			Filament volume fraction in specimens (vol.%)		
		Matrix	Continuous fibers		Matrix	Continuous fibers		Matrix	Continuous fibers	
			Carbon	Kevlar		Carbon	Kevlar		Carbon	Kevlar
Non-hybrid composites	0°-CCFRPA	4	4	-	0.1050	0.0750	-	58.3	41.7	-
	0°-CKFRPA	4	-	4	0.1050	-	0.0625	62.7	-	37.3
	90°-CCFRPA	4	4	-	0.1075	0.0700	-	61.1	38.9	-
	90°-CKFRPA	4	-	4	0.1075	-	0.0575	64.7	-	35.3
	±45°-CCFRPA	4	4	-	0.1150	0.0700	-	62.2	37.8	-
	±45°-CKFRPA	4	-	4	0.1150	-	0.0575	66.7	-	33.3
Hybrid composites	0°-CCFRPA/ 90°-CKFRPA	4	2	2	0.1050	0.0750	0.0625	60.4	21.7	17.9
	90°-CCFRPA/ 0°-CKFRPA	4	2	2	0.1075	0.0700	0.0575	62.8	20.4	16.8
	±45°-CCFRPA/ ±45°-CKFRPA	4	2	2	0.1150	0.0700	0.0575	64.3	19.6	16.1

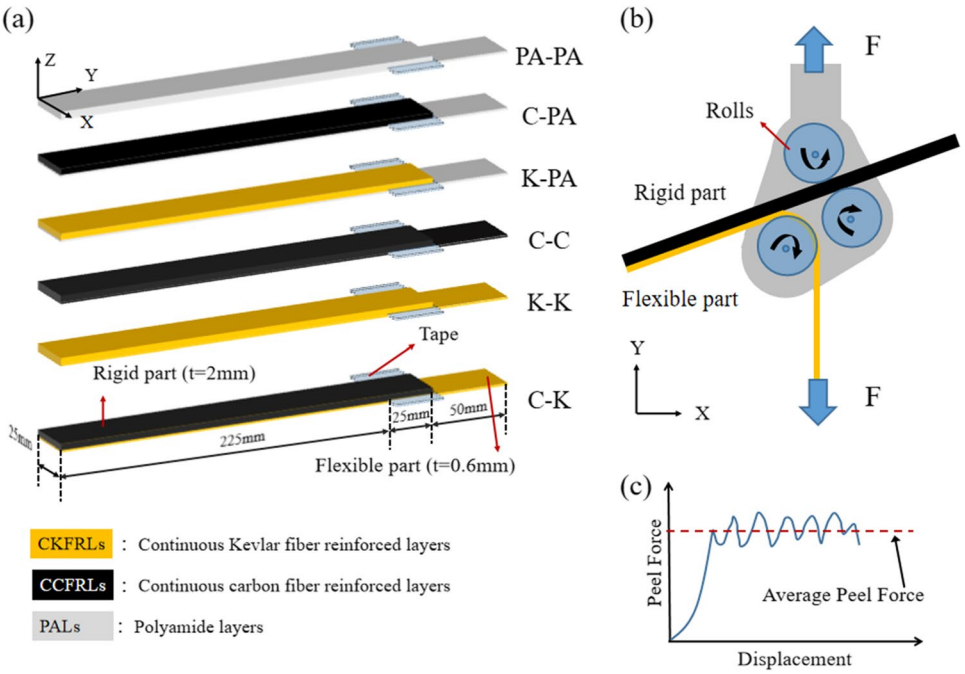

Fig. 2 Schematic presentation of **a** peeling test specimens, **b** peel test set-up, and **c** average peel loads

different interfaces, "PA" stood for PA matrix, and "C" and "K" stood for continuous carbon fiber and continuous Kevlar fiber layers, respectively.

The roller peel tests in the current study were performed to study the adhesion properties of the printed composites by the same MTS universal mechanical testing machine (E44, MTS Co., USA) but with a 1-kN load cell. Figure 2(b) shows the tests set-up of the peeling test. A cross-head loading rate of 100 mm/min was applied at room temperature according to the ASTM D3167 standard. During the test, the peel force and cross head displacement were recorded; thus, the average peel loads were calculated as shown in Fig. 2(c). A total of three specimens were tested in each test condition, and the average values were reported with their standard deviation.

3 Results and discussion

3.1 Tensile properties

To show the mechanical behaviors for the printed non-hybrid and hybrid composites, the tensile stress–strain curves for all the composites are illustrated in Fig. 3 according to their raster orientations and stacking sequences. In Fig. 3, the black lines presented the continuous carbon fiber (CCF)-reinforced composites, and the yellow lines presented the continuous Kevlar fiber (CKF)-reinforced composites. It could be found that the tensile strength of hybrid continuous fiber-filled composites with 0°/90° raster orientations was higher than that of 90° non-hybrid composites but was lower compared to 0° non-hybrid composites whatever the reinforcement fibers were. Besides, ± 45° hybrid composites showed higher tensile strengths than ± 45° single Kevlar fiber-reinforced composites but presented lower strengths compared to ± 45° single carbon fiber-reinforced non-hybrid composites.

These results showed that the simultaneous use of continuous carbon and Kevlar fibers with different raster orientations and sequences could be an effective method to tailor the mechanical behaviors. Therefore, this study investigated the mechanical behaviors for hybrid composites under different parameters in the following parts. For the hybrid composites, taking into account the stacking sequence, the tensile modulus of the SD hybrid composites were higher than those of the CD hybrid composites whatever the fiber type and orientation were. However, the tensile strength of the 0°/90° CD hybrid composites was higher than that of the 0°/90° SD hybrid composites, while the ± 45° CD hybrid composites showed lower strength than the ± 45° SD hybrid composites.

To further understand the damage mode and failure mechanism of hybrid continuous fiber-reinforced composites with different stacking sequences and raster orientations, images of specimens that stretched in different stages (a, b, and c in Fig. 3) were captured. Noted that only ultimate failure (point C) images for the 0°/90° hybrid composites were exhibited, while the strain evolutions (A, B, and C) for the ± 45° hybrid composites were compared because they had different damage modes for two types of stacking sequences. In Figs. 4 and 5, generally, it can be seen that the main failure modes of the printed hybrid composites included delamination

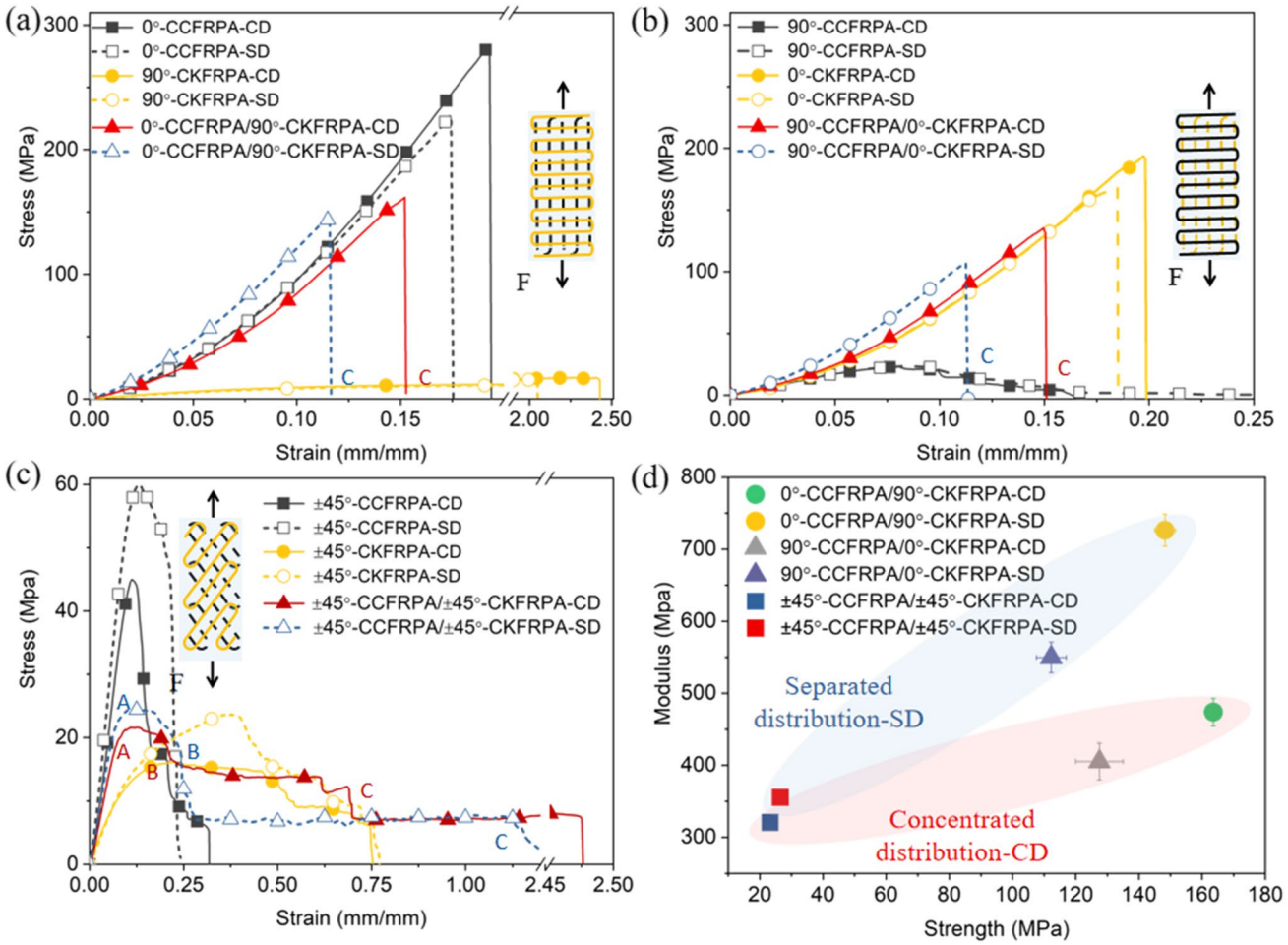

Fig. 3 Effects of raster orientations and stacking sequences on **a**–**c** tensile strain–stress and **d** tensile modulus and strength of 3D printed continuous hybrid fiber-reinforced composites under CD and SD stacking sequences

de-bonding between adjacent filaments and fibers, and matrix breakages near the localized fractured areas.

Figures 4(a) and (b) show the fractured sections of the printed 0°/90° hybrid composites under different stacking sequences. The typical damage mechanisms for the 90°-CCFRPA/0°-CKFRPA composites are schematically shown in Fig. 4(c). We chose 90°-CCFRPA/0°-CKFRPA to show here because the 0°-CCFRPA/90°-CKFRPA hybrid composites displayed similar damage mechanisms.

In Fig. 4(a) and (b), it could be found that the major difference in the damage modes of the 0°/90° composites with two stacking sequences was the way of fiber breakage. Whatever the reinforced continuous fiber was, 0° fiber filament breakages together with splitting were found in composites with CD stacking sequence, while the SD composites only showed 0° fiber breakages. These phenomena perhaps could be attributed to the CD stacking sequence, delaying the cracks' propagation in the composites (see Fig. 4(c)). Specifically, whatever the stacking sequences, the debonding between adjacent 90° fiber filaments first occurred, leading to delamination between adjacent plies around the debonding failures. The cracks then aggregated to 0° fiber plies in CD specimens due to the above delamination, while the 0° fiber plies in SD specimens broke immediately. The 0° continuous fibers in the CD specimens then continued to bear stress near the cracked zone until the breakage and splitting of fibers occurred in the composites. The fiber failure caused out-of-plane normal cracks that occurred in both the CD and SD composites, leading to stress concentration aggregated to PA plies around the failed continuous fibers until the PA ply breakages. These results were perhaps the reasons why the CD composites had higher tensile strength than the SD ones. Meanwhile, less debonding between adjacent 90° fiber filaments were found in the SD composites rather than in the CD composites in the initial linear stage, which could be used to explain why the SD specimens showed a slightly higher tensile modulus compared to the CD specimens. In addition, the damage modes of the 90° fiber filaments in the 0°/90° composites showed a significant difference between the two types of fiber reinforcements. Specifically, the

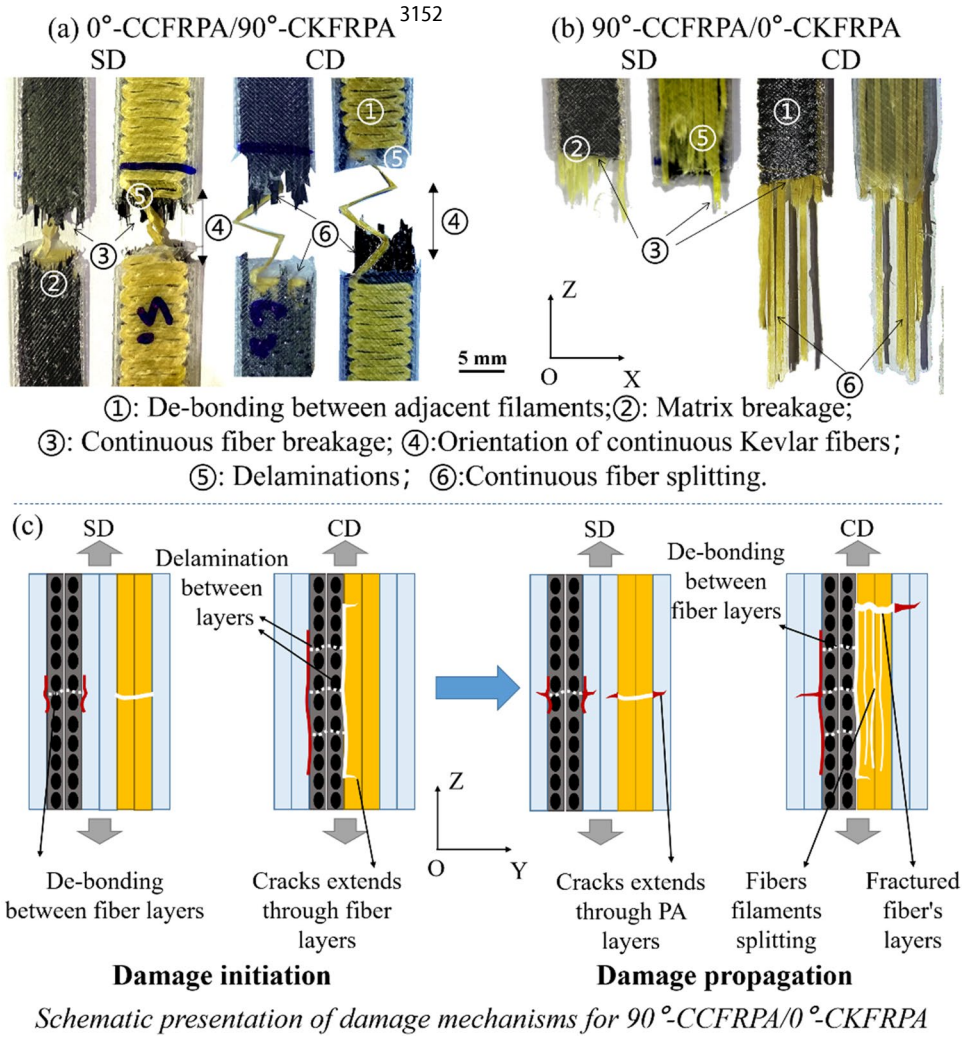

Schematic presentation of damage mechanisms for 90 °-CCFRPA/0 °-CKFRPA

Fig. 4 **a**, **b** Fractured sections and **c** schematic presentation of damage mechanisms for the 3D printed 0°/90° hybrid continuous fiber-reinforced composites with different stacking sequences

90° carbon fiber breakages for 90°-CCFRPA/0°-CKFRPA were easy to be observed, while the 90° continuous Kevlar fibers in 0°-CCFRPA/90°-CKFRPA were oriented to the stretching direction with limited breakage in our study range, leading to the slightly high tensile toughness but low tensile strength of 0°-CCFRPA/90°-CKFRPA compared to 90°-CCFRPA/0°-CKFRPA.

Figure 5(a) shows the damage evolution for the ±45° composites captured by a digital camera at points A, B, and C marked in Fig. 3(c). In this figure, point A corresponded to the initial damage stage, while points B and C represented the damage evolution stages. In the initial stage, whatever the staking sequences and reinforcements were, debonding (white lines in Fig. 5(b)) between adjacent continuous fiber filaments was discovered in all the ±45° composites. The continuous fiber filaments were observed to debond first, perhaps because they had weaker interfacial bonding than the PA matrix [12]. Compared to the SD specimens, a larger number of debonding in the CD specimens was found, resulting in the lower tensile modulus of the CD specimens than that of the SD specimens. In the damage propagation stage at point B, delamination, slight PA ply fractures, and continuous carbon fiber filament breakages were found in the CD composites, while PA breakages were not easy to be observed in the SD composites. It was probably the reason why the SD specimens showed higher tensile stress than the CD specimens at a strain range of 0.25 to 0.75. This phenomenon suggested that the separated sequence of the continuous fiber in the composites retarded the debonding and crack propagations through the whole specimen, further delaying the delamination between fiber-PA interfaces and microcracking initiation in PA plies, resulting in the higher tensile strength of the SD specimens compared to the CD specimens. Finally, at point C, PA ply fractures were found in all the composites. In addition, the Kevlar fibers in both the CD and SD specimens were orientated along the tensile direction without breakages, which enhanced the elongation at the break of the composites.

Energy absorption capability is a key index for materials applied to collision protection structures [30, 31]. To

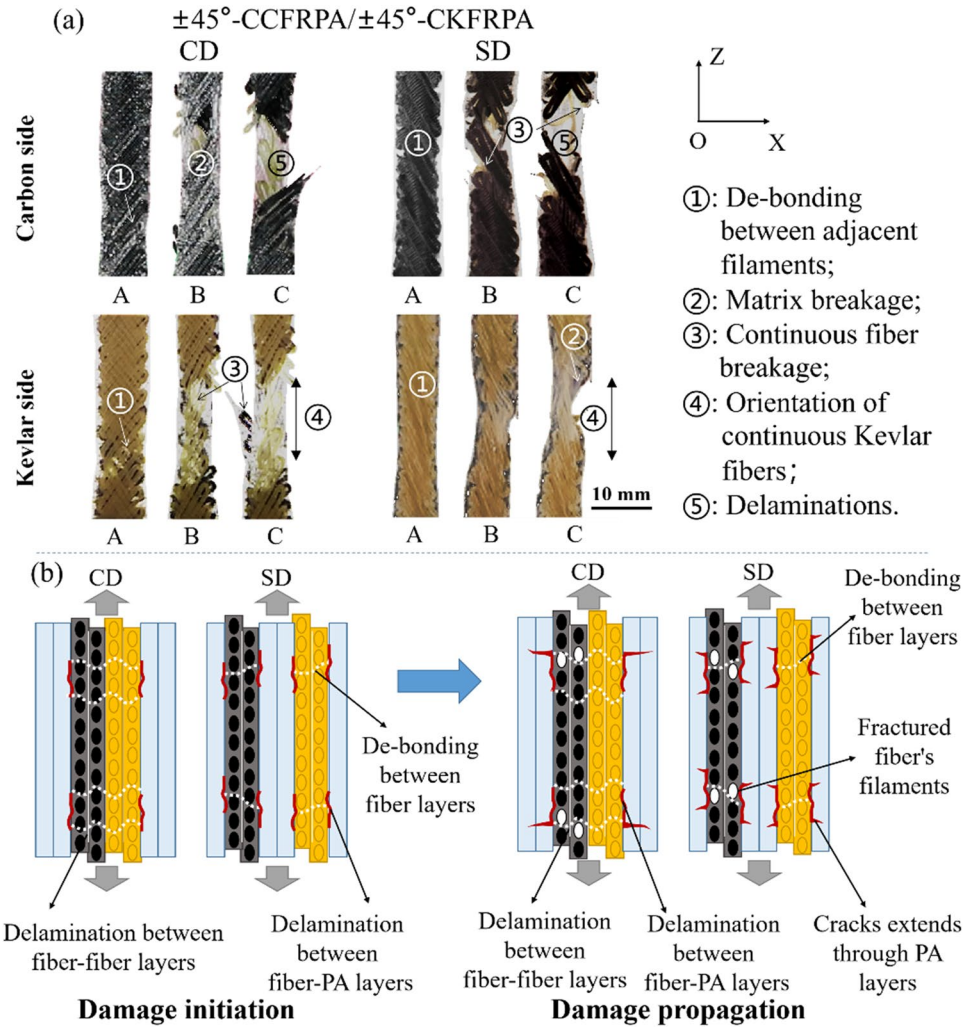

Fig. 5 **a** Fractured sections and **b** schematic presentation of damage mechanisms for 3D printed ± 45° hybrid continuous fiber-reinforced composites with different stacking sequences

investigate the influence of interfaces induced by the stacking sequence on the energy absorption capability of the printed hybrid continuous fiber-filled composites and to quantify the contribution of each fiber to hybrid composites, we studied the hybrid effect based on the energy absorption capability of the hybrid composites with different stacking sequences and raster orientations.

3.2 Hybrid effect

Hybridization using different reinforcements is one of the effective ways to increase the energy absorption capability of composites. By tailoring the filler, matrix, and structural parameters, it is possible to control and design hybrid composites with balanced or specific properties. A positive or negative hybrid effect for composites could be achieved according to their compositions by the rule of mixture (*RoM*) [32, 33].

The present study handled the absorbed energies of the printed composites to investigate the variation of the hybrid effect by performing the rule of mixture. The resulting degree of the hybrid effect (h_e) was calculated from Eqs. (1) and (2):

$$E_{(\mathrm{RoM})} = \frac{1}{2}\left(E_C + E_K\right) \tag{1}$$

where the E_C and E_K are the absorbed energy values through the tensile test of non-hybrid composites (CCFRPA and CKFRPA), respectively. $E_{(\mathrm{RoM})}$ indicates the resulting rule of mixture values of absorbed energy for non-hybrid composites, and

$$h_e = \frac{E_h}{E_{(\mathrm{RoM})}} - 1 \tag{2}$$

whereE_h is the absorbed energy value of the hybrid continuous fiber-reinforced composites. A positive or negative hybrid effect could be obtained according to Eq. (3):

$$\begin{aligned} &h_e > 0, \text{positive hybrid effect} \\ &h_e < 0, \text{negative hybrid effect} \end{aligned} \tag{3}$$

The hybrid effects of the printed composites with different stacking sequences and raster orientations as a function of strain are shown in Fig. 6. In this figure, the 0°/90° hybrid composites showed a positive hybrid effect before the strain of 0.20 mm/mm that was probably due to the significantly high energy absorption rate while displaying a negative effect after the strain of 0.20 mm/mm, which was attributed to the lower energy absorption capabilities. The 0°/90° hybrid composites may be applied in energy absorption composites where high energy absorption capability is needed within relatively small deformations.

For the ±45° hybrid composites, as shown in Fig. 6(c) and (f), a negative hybrid effect was found in the ±45° CD hybrid composites from 0 to 0.25 mm/mm, while a positive effect was observed after the strain of 0.25 mm/mm. The ±45° SD composites showed a negative hybrid effect from 0 to 1.00 mm/mm while illustrating a positive effect from 1.00 to 1.25 mm/mm. Besides, $h_e(CD)$ was higher than $h_e(SD)$ at the end of the tests, which was attributed to the stacking sequence of the continuous fibers for the composites, affecting the mechanical properties of the structure. The ±45° CD hybrid composites therefore could be used for structural parts with a high energy absorption capability requirement within large deformations.

3.3 Interfacial behaviors

In this study, the adhesion properties of different interfaces in printed hybrid composites were evaluated using floating roller peel tests. Figure 7 shows the representative peel force–displacement curves for various laminated composites in the peeling tests. In Fig. 7, the peel forces for all the composites fluctuated steadily after initial rising. However, the forces for the PA-PA interface dropped suddenly after a 20-mm displacement. The average peel loads were determined along the 100-mm peeling length ranging from 20 to 120 mm, abandoning the first 20-mm displacement (except for the PA-PA interface) [34, 35]. According to this method (see Fig. 2(c)), the average peel loads for PA-PA were higher than those for C–C, followed by C-K, K-K, C-PA, and K-PA.

4 Prediction model

As discussed above, the interfaces played a non-ignorable role in the tensile behavior of printed hybrid continuous fiber composites. An analytical model considering interface contribution was therefore essential to be established. Here, the PA-PA interface's peeling force (F_{PA-PA}) was used as a correlative value, and the ratios of other interfaces' peeling forces (F_x) to that of F_{PA-PA} were used as the strengthening coefficient,$a^*(x)$, estimated from the following equation (x represented interfaces including interface matrix–matrix, interface matrix-fiber, and interface fiber–fiber), and the values are listed in Fig. 8.

$$a^*(x) = \frac{F_x}{F_{PA-PA}} (x = PA-PA, C-C, K-K, C-K, C-PA \text{ and } K-PA) \quad (4)$$

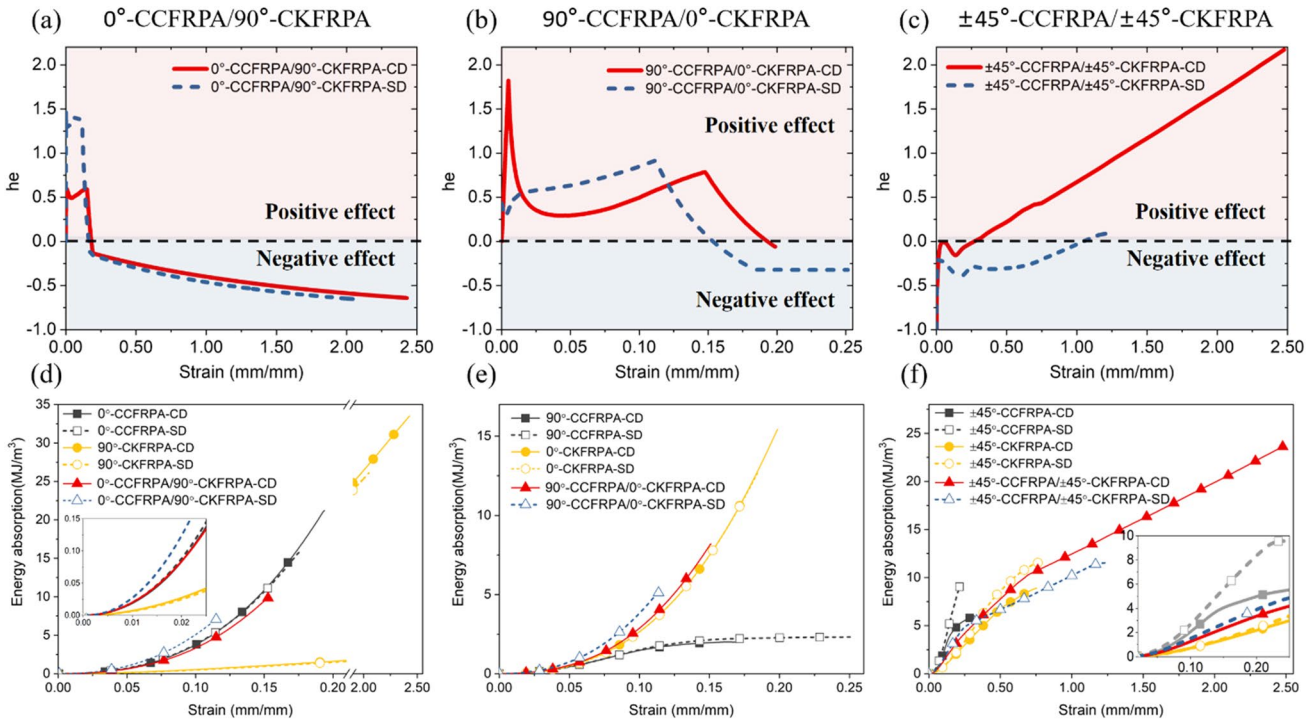

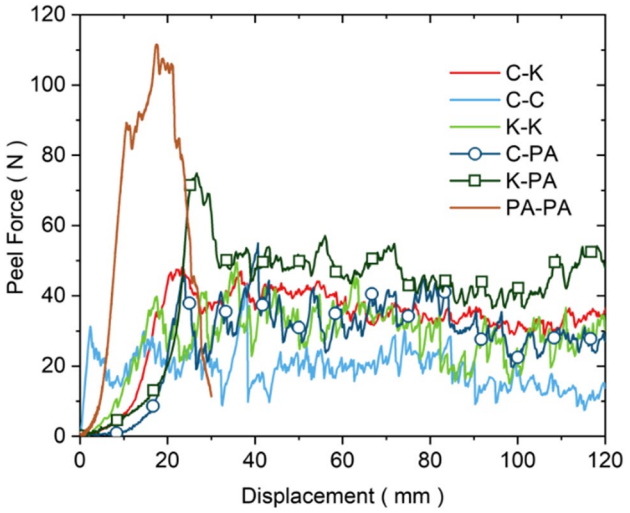

Fig. 7 Interlaminar force–displacement curves for 3D printed continuous fiber-reinforced composites

Then, this strengthening coefficient, $a^*(x)$, was incorporated into the volume average stiffness (VAS) approach to compute the stiffness Q of the composites based on the stiffness of the matrix and continuous fiber as follows (note that the strengthening coefficients $a^*(x)_m$ and $a^*(x)_f$ were assumed to evenly contribute to adjacent printed matrix layers and continuous fiber layers, respectively):

$$\begin{cases} Q = Q'_m + Q'_f \\ Q'_m = \sum_{i=1}^{n_m} a^*(x)_{mi} V_{mi} \overline{Q}_{mi} (n_m = \text{the number of matrix plies}) \\ Q'_f = \sum_{j=1}^{n_f} a^*(x)_{fj} V_{fj} \overline{Q}_{fj} (n_f = \text{the number of fiber plies}) \end{cases} \tag{5}$$

where V_{mi} and V_{fj}, respectively, meant the volume fractions of each matrix (PA) layer and continuous fiber layer, and details of volume fraction for the continuous fiber and matrix

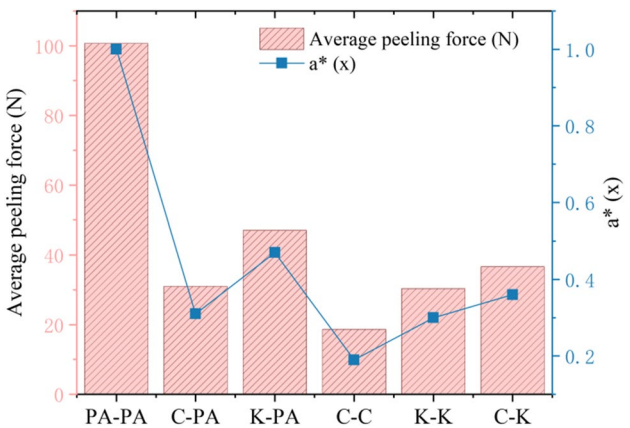

Fig. 8 Average peeling force and strengthening coefficient for the 3D printed continuous fiber-reinforced composites

Table 2 Adopted elastic properties of each component for the printed materials [36]

Material properties	Carbon	Kevlar	PA
Longitudinal elastic modulus E_1 (MPa)	85,000	30,000	380
Transverse elastic modulus E_2 (MPa)	26,000	10,000	380
In-plane shear modulus G_{12} and G_{23} (MPa)	5000	5000	141
Poisson's ratio ν_{12}	0.3	0.2	0.35

in the composites are given in Table 1. $\overline{Q}_m$ and $\overline{Q}_f$ were, respectively, the stiffness of the matrix and fibers in the global coordinate system, and were related to the Q_m and Q_f in the fiber coordinate systems as

$$\overline{Q}_m = [T]^T Q_m [T] \tag{6}$$

$$\overline{Q}_f = [T]^T Q_f [T] \tag{7}$$

where the stiffness of the matrixQ_m, stiffness of fiber Q_f, and transformation matrix [T] were defined as follows [36]:

$$Q_m = \begin{bmatrix} \frac{E}{1-\nu^2} & \frac{\nu E}{1-\nu^2} & 0 \\ \frac{\nu E}{1-\nu^2} & \frac{E}{1-\nu^2} & 0 \\ 0 & 0 & G \end{bmatrix} \tag{8}$$

$$Q_f = \begin{bmatrix} \frac{E_1}{1-\nu_{12}\nu_{21}} & \frac{\nu_{12}E_2}{1-\nu_{12}\nu_{21}} & 0 \\ \frac{\nu_{12}E_2}{1-\nu_{12}\nu_{21}} & \frac{E_2}{1-\nu_{12}\nu_{21}} & 0 \\ 0 & 0 & G_{12} \end{bmatrix} \tag{9}$$

$$[T] = \begin{bmatrix} \cos^2\theta & \sin^2\theta & \sin\theta\cos\theta \\ \sin^2\theta & \cos^2\theta & -\sin\theta\cos\theta \\ \sin\theta\cos\theta & -\sin\theta\cos\theta & \cos^2\theta - \sin^2\theta \end{bmatrix} \tag{10}$$

where θ was the angle of the matrix and fibers;E, G, and ν were, respectively, the elastic modulus, shear modulus, and Poisson's ratio of the matrix;E_1,E_2,G_{12}, and ν_{12} were, respectively, the elastic modulus, shear modulus, and Poisson's ratio of fibers, and the values are given in Table 2.

The elastic modulus, E_{11}, of the composites can be obtained from the components of the compliance matrix [S] as

$$E_{11} = \frac{1}{S_{11}} \tag{11}$$

where S_{11} was the components of the compliance matrix [S], which was the inversion of the stiffness matrix [Q] given in Eq. (5).

Figure 9 displays the comparison results of the elastic modulus obtained from experimental data and the proposed model with the consideration of interfaces contribution. In

this figure, it can be seen that our proposed model considering interface contribution could well estimate the elastic modulus for hybrid composites with different staking sequences and fiber raster orientations by showing small gaps between the experimental and computed results. Meanwhile, the computed results were dependent on the designed configuration of continuous fiber's raster orientations. The reasons for the discrepancy were drawn and as follows:

1. First, the discrepancy may come from the taking of the fixed peel force, F_x, from the 0° specimens for calculating the interface strengthening coefficient. Though the average peel forces of the 0° peeling specimens were almost the mean value for the average peel force of the 0°, 90°, and 45° specimens, there was still a difference in the peel force between the specimens with 0° continuous carbon fibers and other raster orientations' specimens. Specifically, it could be found that in Eq. (4) to (11), a higher F_x led to a higher $a^*(x)$, which finally led to a higher computed tensile modulus. The peel force F_x of the 0° specimens was higher than that of the 90° specimens but slightly lower compared to that of the 45° specimens. Thus, the computed results for the 90° specimens were higher, but those for the 45° specimens were lower. For example, the computed result of 0° CCFRPA/90°CKFRPA-SD was about 13.3% higher than that of the experimental result. In contrast, the predicted tensile modulus of the ± 45°CCFRPA/ ± 45°CKFRPA-SD specimen was about 6.0% lower than that of the experimental modulus.
2. In addition, these discrepancies may also come from the assumed even contribution of the interface strengthening coefficient between adjacent layers. In the current study, the interfacial strengthening coefficient was assumed to evenly contribute to adjacent printed layers. However, as the material contribution to the interface could be different, the interface close to different materials should have different properties. This may be another reason that results in the discrepancies between the computed modulus and the experimental modulus of our studied materials.

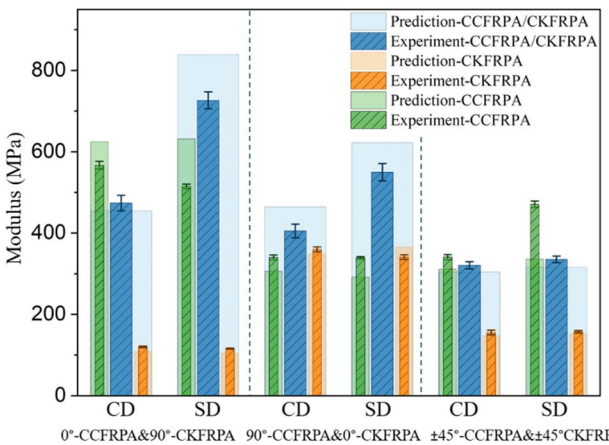

Fig. 9 Comparison of the experimentally measured and predicted elastic modulus by using the prediction model

5 Conclusions

In this study, the mechanical behaviors of 3D printed continuous non-hybrid and hybrid fiber-filled composites with different reinforcement fibers, stacking sequences, as well as raster orientations were evaluated. A morphological investigation was applied to reveal the deformation and failure mechanisms of printed hybrid continuous fiber-reinforced composites. A hybrid effect model was developed to analyze the hybrid effect based on the energy absorption capabilities of composites. The interfacial strengths between different materials were investigated by roller peeling test. An analytical approach was introduced to predict the stiffness behavior of the printed composites. The following conclusions were drawn from this study:

1. Simultaneous use of continuous carbon and Kevlar fibers with different raster orientations and sequences could be an effective method to tailor rigidity and ductility and to achieve higher mechanical performance.
2. The stacking sequences induced by designed interfaces between different material layers played an important role in the mechanical properties of the printed composites. The hybrid composite specimens with SD sequence showed a higher tensile modulus than that the CD hybrid composites because the SD sequence could delay crack initiation and propagation.
3. The 0°/90° hybrid composites showed a positive hybrid effect at relatively small strain, which could be applied in an energy absorption structure where high energy absorption capability is needed within relatively small deformations. In contrast, the ± 45° CD hybrid composites exhibited a positive hybrid effect at relatively large strain, which could be used for structural parts with a high energy absorption capability requirement within large deformations.
4. The prediction properties of 3D printed continuous non-hybrid and hybrid fiber-filled composites with different reinforcements, stacking sequences, and raster orientations were in good agreement with the experimental results.

Future works will be necessary to analyze the interface bonding quality of hybrid continuous fiber-reinforced composites in different printing parameters and configurations.

Nevertheless, these results gave a database that can be useful for further industrial development of 3D printed continuous composites, in particular to enrich finite element models for designing optimized structures.

Author contributions All the authors contributed to the study conception and design. Conceptualization: Kui Wang and Said Ahzi; data curation and methodology: Shixian Li; resources: Yong Peng; software: Wanying Zhu; writing (original draft): Shixian Li; writing (review and editing): Kui Wang and Francisco Chinesta. All the authors commented on previous versions of the manuscript. All the authors read and approved the final version of the manuscript.

Funding Author Kui Wang would like to acknowledge the National Natural Science Foundation of China (No. 51905555), the Hu-Xiang Youth Talent Program (2020RC3009), and the Innovation-Driven Project of Central South University (No. 2019CX017) for supporting the experimental research in this work.

Declarations

Ethical approval No ethical approval was required for this research

Consent to participate Not applicable.

Consent for publication All authors have read and agreed to the published version of the manuscript.

Competing interests The authors declare no competing interests.

References

1. Pan Y, Zhang Y, Zhang D, Song Y (2021) 3D printing in construction: state of the art and applications. Int J Adv Manuf Technol 115(5):1329–1348. https://doi.org/10.1007/s00170-021-07213-0
2. Rinaldi M, Ghidini T, Cecchini F, Brandao A, Nanni F (2018) Additive layer manufacturing of poly(ether ether ketone) via FDM. Compos B Eng 145:162–172. https://doi.org/10.1016/j.compositesb.2018.03.029
3. Tamir TS, Xiong G, Fang Q, Dong X, Shen Z, Wang F-Y (2022) A feedback-based print quality improving strategy for FDM 3D printing: an optimal design approach. Int J Adv Manuf Technol 120(3):2777–2791. https://doi.org/10.1007/s00170-021-08332-4
4. McLouth TD, Severino JV, Adams PM (2017) Patel DN, Zaldivar RJ. The impact of print orientation and raster pattern on fracture toughness in additively manufactured ABS. Addit Manuf 18:103–109. https://doi.org/10.1016/j.addma.2017.09.003
5. Rao Y, Wei N, Yao S, Wang K, Peng Y (2021) A process-structure-performance modeling for thermoplastic polymers via material extrusion additive manufacturing. Addit Manuf 39:101857. https://doi.org/10.1016/j.addma.2021.101857
6. Wang P, Zou B, Ding S, Huang C, Shi Z, Ma Y, Yao P (2020) Preparation of short CF/GF reinforced PEEK composite filaments and their comprehensive properties evaluation for FDM-3D printing. Compos B Eng 198:108175. https://doi.org/10.1016/j.compositesb.2020.108175
7. Mei H, Ali Z, Ali I, Cheng L (2019) Tailoring strength and modulus by 3D printing different continuous fibers and filled structures into composites. Adv Compos Hybrid Mater 2(2):312–319. https://doi.org/10.1007/s42114-019-00087-7
8. Van Der Klift F, Koga Y, Todoroki A, Ueda M, Hirano Y, Matsuzaki R (2016) 3D printing of continuous carbon fibre reinforced thermo-plastic (CFRTP) tensile test specimens. Open J Compos Mater 6(1):18–27. https://doi.org/10.4236/ojcm.2016.61003
9. Heidari-Rarani M, Rafiee-Afarani M, Zahedi A (2019) Mechanical characterization of FDM 3D printing of continuous carbon fiber reinforced PLA composites. Compos B Eng 175:107147. https://doi.org/10.1016/j.compositesb.2019.107147
10. Dickson AN, Barry JN, McDonnell KA, Dowling DP (2017) Fabrication of continuous carbon, glass and Kevlar fibre reinforced polymer composites using additive manufacturing. Addit Manuf 16:146–152. https://doi.org/10.1016/j.addma.2017.06.004
11. Wang K, Long H, Chen Y, Baniassadi M, Rao Y, Peng Y (2021) Heat-treatment effects on dimensional stability and mechanical properties of 3D printed continuous carbon fiber-reinforced composites. Compos A: Appl Sci Manuf 147:106460. https://doi.org/10.1016/j.compositesa.2021.106460
12. Wang F, Wu J, Hu L, Yu C, Wang B, Huang X, Miller K, Wittek A (2022) Evaluation of the head protection effectiveness of cyclist helmets using full-scale computational biomechanics modelling of cycling accidents. J Safety Res 80:109–134. https://doi.org/10.1016/j.jsr.2021.11.005
13. Fotouhi M, Damghani M, Leong MC, Fotouhi S, Jalalvand M, Wisnom MR (2020) A comparative study on glass and carbon fibre reinforced laminated composites in scaled quasi-static indentation tests. Compos Struct 245:112327. https://doi.org/10.1016/j.compstruct.2020.112327
14. Fotouhi S, Clamp J, Bolouri A, Pozegic TR, Fotouhi M (2019) Investigating polyethersulfone interleaved glass/carbon hybrid composite under impact and its comparison with GLARE. Compos Struct 226:111268. https://doi.org/10.1016/j.compstruct.2019.111268
15. Bulut M, Erkliğ A, Yeter E (2019) Hybridization effects on quasi-static penetration resistance in fiber reinforced hybrid composite laminates. Compos B Eng 98:9–22. https://doi.org/10.1016/j.compositesb.2016.05.025
16. Wang K, Li S, Rao Y, Wu Y, Peng Y, Yao S, Zhang H, Ahzi S (2019) Flexure behaviors of ABS-based composites containing carbon and Kevlar fibers by material extrusion 3D printing. Polymers 11(11):1878. https://doi.org/10.3390/polym11111878
17. Wang K, Li S, Wu Y, Rao Y, Peng Y (2021) Simultaneous reinforcement of both rigidity and energy absorption of polyamide-based composites with hybrid continuous fibers by 3D printing. Compos Struct 267:113854. https://doi.org/10.1016/j.compstruct.2021.113854
18. Peng Y, Wu Y, Li S, Wang K, Yao S, Liu Z, Garmestani H (2020) Tailorable rigidity and energy-absorption capability of 3D printed continuous carbon fiber reinforced polyamide composites. Compos Sci Technol 199:108337. https://doi.org/10.1016/j.compscitech.2020.108337
19. Yavas D, Zhang Z, Liu Q, Wu D (2021) Interlaminar shear behavior of continuous and short carbon fiber reinforced polymer composites fabricated by additive manufacturing. Compos B Eng 204:108460. https://doi.org/10.1016/j.compositesb.2020.108460
20. Touchard F, Chocinski-Arnault L, Fournier T, Magro C, Lafitte A, Caradec A (2021) Interfacial adhesion quality in 3D printed continuous CF/PA6 composites at filament/matrix and interlaminar scales. Compos B Eng 218:108891. https://doi.org/10.1016/j.compositesb.2021.108891
21. Ming Y, Zhang S, Han W, Wang B, Duan Y, Xiao H (2020) Investigation on process parameters of 3D printed continuous carbon fiber-reinforced thermosetting epoxy composites. Addit Manuf 33:101184. https://doi.org/10.1016/j.addma.2020.101184

22. Cheng P, Wang K, Chen X, Wang J, Peng Y, Ahzi S, Chen C (2021) Interfacial and mechanical properties of continuous ramie fiber reinforced biocomposites fabricated by in-situ impregnated 3D printing. Ind Crops Prod 170:113760. https://doi.org/10.1016/j.indcrop.2021.113760
23. Li N, Link G, Jelonnek J (2020) 3D microwave printing temperature control of continuous carbon fiber reinforced composites. Compos Sci Technol 187:107939. https://doi.org/10.1016/j.compscitech.2019.107939
24. Araya-Calvo M, López-Gómez I, Chamberlain-Simon N, León-Salazar JL, Guillén-Girón T, Corrales-Cordero JS, Sánchez-Brenes O (2018) Evaluation of compressive and flexural properties of continuous fiber fabrication additive manufacturing technology. Addit Manuf 22:157–164. https://doi.org/10.1016/j.addma.2018.05.007
25. Parmiggiani A, Prato M, Pizzorni M (2021) Effect of the fiber orientation on the tensile and flexural behavior of continuous carbon fiber composites made via fused filament fabrication. Int J Adv Manuf Technol 114(7):2085–2101. https://doi.org/10.1007/s00170-021-06997-5
26. Chacón J, Caminero M, García-Plaza E, Núñez P (2017) Additive manufacturing of PLA structures using fused deposition modelling: effect of process parameters on mechanical properties and their optimal selection. Mater Des 124:143–157. https://doi.org/10.1016/j.matdes.2017.03.065
27. Chacón J, Caminero M, Núñez P, García-Plaza E, García-Moreno I, Reverte J (2019) Additive manufacturing of continuous fibre reinforced thermoplastic composites using fused deposition modelling: effect of process parameters on mechanical properties. Compos Sci Technol 181:107688. https://doi.org/10.1016/j.compscitech.2019.107688
28. Pascual-González C, Iragi M, Fernández A, Fernández-Blázquez JP, Aretxabaleta L, Lopes CS (2020) An approach to analyse the factors behind the micromechanical response of 3D-printed composites. Compos B Eng 186:107820. https://doi.org/10.1016/j.compositesb.2020.107820
29. Iragi M, Pascual-González C, Esnaola A, Lopes C, Aretxabaleta L (2019) Ply and interlaminar behaviours of 3D printed continuous carbon fibre-reinforced thermoplastic laminates: effects of processing conditions and microstructure. Addit Manuf 30:100884. https://doi.org/10.1016/j.addma.2019.100884
30. Mahesh V, Joladarashi S, Kulkarni SM (2021) Damage mechanics and energy absorption capabilities of natural fiber reinforced elastomeric based bio composite for sacrificial structural applications. Defence Technology 17(1):161–176. https://doi.org/10.1016/j.dt.2020.02.013
31. Kumar AP, Maneiah D, Sankar LP (2021) Improving the energy-absorbing properties of hybrid aluminum-composite tubes using nanofillers for crashworthiness applications. Proc Inst Mech Eng C J Mech Eng Sci 235(8):1443–1454. https://doi.org/10.1177/0954406220942267
32. Bulut M, Erkliğ A (2018) The investigation of quasi-static indentation effect on laminated hybrid composite plates. Mech Mater 117:225–234. https://doi.org/10.1016/j.mechmat.2017.11.005
33. Marom G, Fischer S, Tuler F, Wagner H (1978) Hybrid effects in composites: conditions for positive or negative effects versus rule-of-mixtures behaviour. J Mater Sci 13(7):1419–1426. https://doi.org/10.1007/BF00553194
34. Arouche MM, Budhe S, Banea MD, Teixeira de Freitas S, de Barros S (2019) Interlaminar adhesion assessment of carbon-epoxy laminates under salt water ageing using peel tests. Proc Inst Mech Eng L 233(8):1555–1563. https://doi.org/10.1177/1464420718766626
35. Kubit A, Trzepieciński T, Krasowski B, Slota J, Spišák E (2020) Strength analysis of a rib-stiffened GLARE-based thin-walled structure. Materials 13(13):2929. https://doi.org/10.3390/ma13132929
36. Al Abadi H, Thai H-T, Paton-Cole V, Patel V (2018) Elastic properties of 3D printed fibre-reinforced structures. Compos Struct 193:8–18. https://doi.org/10.1016/j.compstruct.2018.03.051